
Block-Wise Differentiable Sinkhorn Attention: Tail-Refinement Gradients with a Single-Active-Dustbin Bridge

Dylan B. Forde
Independent Researcher
forde.dylan@gmail.com

Abstract

We study long-context balanced entropic optimal transport (OT) attention on TPU hardware through a stopped-base, fixed-depth tail-refinement surrogate. After a stopped T -step Sinkhorn solve, we unroll a short refinement tail and differentiate that surrogate exactly. For the reported $R = 2$ TPU path, the backward pass contains four staircase plan factors. We prove an exact one-reference-tile schedule: the $R = 2$ score cotangent is a single reference plan tile times an explicit modifier field built from vector cotangents and dual differences. This yields block-wise cost $O((T + R)LW)$, $O(Ld)$ input storage, and $O(L)$ additional HBM usage for fixed head dimension d and band width W on the balanced fixed-support path. We also formalize the current `dustbin_block` path as the same unit-target surrogate on an augmented support, so the adjoint schedule lifts to the single-active-dustbin path used in our TPU runs; this bridge is algebraic and does not claim a general KL-unbalanced or arbitrary-capacity gap model. We provide a local surrogate-bias bound, an a posteriori bias certificate, and a projective contraction certificate for strictly positive active blocks. On synthetic masked problems, the optimized kernel matches exact autodiff of the same centered surrogate to within 10^{-5} – 10^{-10} . On TPU v6e-8, a four-configuration Pfam screen completes end-to-end, and a promoted balanced $R = 2$ run sustains roughly 8.5 examples per second through a three-hour budget, reaching step 1437. Held-out Pfam test shards improve reconstruction from 5.57 to 2.05 and sparse CE from 5.53 to 5.30 relative to step 0, with CE logged diagnostically rather than optimized directly; target-barycenter alignment metrics do not materially improve, and a deterministic diagonal reference remains stronger on those metrics. These results support exact fixed-depth backward theory, centered-kernel validation, and scoped trainability evidence for the reported TPU path.

1 Introduction

Pairwise alignment and structural matching remain central problems for sequence modeling. Classical dynamic-programming methods such as Smith–Waterman [Smith and Waterman, 1981] provide optimal alignments but are not differentiable, so they cannot be inserted directly into end-to-end neural architectures. Entropic optimal transport (OT) offers a natural differentiable relaxation [Cuturi, 2013, Peyré and Cuturi, 2019]: it replaces a discrete assignment with a smooth transport plan computed by Sinkhorn scaling.

For long-context models, however, two bottlenecks dominate. First, dense OT attention materializes $L \times L$ scores or plans, which is prohibitive at large L . Second, backward-pass design is difficult. Exact autodiff through many Sinkhorn steps is expensive and memory-hungry, while implicit differentiation can require large and unstable linear solves [Luise et al., 2018, Bai et al., 2019]. The key question is

therefore not only how to make OT attention differentiable, but how to make its differentiated object explicit, exact for the surrogate actually used, and compatible with accelerator kernels.

We address this with a stopped-base, fixed-depth *tail-refinement surrogate*. After a stopped T -step balanced Sinkhorn solve, we append a short differentiable tail of depth R and differentiate that surrogate exactly. The reported TPU path uses $R = 2$. A direct implementation of the exact $R = 2$ adjoint must evaluate four distinct staircase plan factors. The signature implementation observation of the paper is that these factors lie in a single row/column scaling orbit, so each block can be evaluated from one reference transport tile plus vector modifiers, avoiding separate plan-tile formation for the remaining three terms.

Single-active-dustbin bridge. The central factorization is balanced and fixed-support. The first extension carried in the unified manuscript is intentionally narrow: the current `dustbin_block` path is not treated as a new OT solver, but as the same unit-target surrogate on an augmented state space with one active dustbin token per side. This keeps the implemented dustbin path inside the algebraic orbit of the main factorization, while leaving general gap-capacity and KL-unbalanced transport models to future work.

Related context. Our work is closest in spirit to recent efforts to make OT-style attention practical at accelerator scale, including FlashSinkhorn [Ye et al., 2026]. The comparison separates along two axes. FlashSinkhorn is an IO-aware solver for streaming entropic OT updates; our contribution is the differentiated stopped-base backward object. In particular, a direct $R = 2$ adjoint must evaluate four distinct staircase plan factors, whereas our transport-orbit calculus evaluates each block from one reference transport tile plus vector modifiers. This does not replace a direct solver-level benchmark against FlashSinkhorn, a matched trained-attention baseline, or a direct four-plan-adjoint TPU benchmark. Fair Pfam comparisons must match the sampler, projection, objective, mask, evaluator, and runtime; the current bundle does not contain a FlashSinkhorn-on-Pfam adapter, trained attention checkpoint, or TPU direct-adjoint result. We therefore treat those as pending benchmarks rather than negative results and do not claim wall-clock dominance. The present paper instead establishes the exact factorized backward object and its TPU realization on the alignment stack used in our experiments. The approach is also complementary to long-context transformer architectures that obtain efficiency through structured sparsity rather than transport constraints, such as Longformer [Beltagy et al., 2020] and BigBird [Zaheer et al., 2020].

The paper makes three main contributions:

- an explicit balanced fixed-support tail-refinement surrogate together with its exact $R = 2$ adjoint and one-reference-tile backward schedule;
- a theorem-aligned single-active-dustbin augmentation showing that the current dustbin transport path is the same unit-target surrogate on an enlarged state space;
- an empirical bridge from exactness validation to TPU-scale training, comprising a completed four-configuration Pfam screen, a promoted long-budget balanced run, and a held-out checkpoint evaluation on Pfam test shards.

2 Method

2.1 Forward Pass: Block-Wise Balanced Sinkhorn

Let Q, K, V be query, key, and value tensors with head dimension d , and let Ω denote a fixed active support with band width W . We absorb the entropic temperature ε into the score matrix

$$S_{ij} = \frac{Q_i K_j^\top}{\sqrt{d} \varepsilon}.$$

The stopped base solve and the refinement tail both use the same masked balanced half-steps

$$u_i^{(t+1)} = -\log \left[\sum_{j:(i,j) \in \Omega} \exp(S_{ij} + v_j^{(t)}) \right], \tag{1}$$

$$v_j^{(t+1)} = -\log \left[\sum_{i:(i,j) \in \Omega} \exp(S_{ij} + u_i^{(t+1)}) \right]. \tag{2}$$

These are unit-target updates: each active row and active column target mass is one. When the active row and column counts are equal, this is the usual compatible balanced OT normalization. On rectangular masked Pfam examples, the implementation still uses this same unit-target Sinkhorn attention map; it should be read as the differentiable transport surrogate actually evaluated by the code, not as a compatible-marginal balanced OT problem with unequal total masses. The implementation computes these updates in tiles, in the same spirit as IO-aware attention kernels. For fixed band width W , a T -step base solve followed by an R -step tail has cost $O((T+R)LW)$ time, $O(Ld)$ input storage, and $O(L)$ additional HBM usage.

Remark 1 (Fixed-Budget ε -Scaling). *The implementation optionally uses a short continuation schedule $\varepsilon_1 \geq \dots \geq \varepsilon_S = \varepsilon$ during the stopped base solve. If the stage iteration counts satisfy $\sum_{s=1}^S T_s = T$, the asymptotic cost remains $O(TLW)$ time and $O(L)$ additional HBM memory for fixed head dimension.*

2.2 Balanced Tail Refinement and the $R = 2$ Staircase

Let $(u^{(0)}, v^{(0)})$ be the stopped potentials produced by the base T -step solve. The differentiated object is not the full T -step map; it is the fixed-depth surrogate

$$\tilde{O}^{[R]}(Q, K, V; u^{(0)}, v^{(0)}) = \mathcal{A}(Q, K, V, u^{(R)}, v^{(R)}),$$

where the refinement iterates are recomputed from the stopped base pair. The implementation stores centered dual representatives for numerical stability, while the main algebra is written in ungauged coordinates. Appendix A gives the corresponding centered gauge ledger: same-time plans are gauge-invariant, while mixed-time centered plans require explicit scalar gauge factors when translated back to ungauged coordinates. The terminal transport application is

$$\mathcal{A}(Q, K, V, u, v)_i = \sum_{j:(i,j) \in \Omega} P_{ij}(u, v) V_j, \quad P_{ij}(u, v) = \exp(S_{ij} + u_i + v_j).$$

There is no extra row renormalization in the training output. Reconstruction uses this raw transport output, sparse CE logs the target-entry transport mass, and row-normalized barycenters are used only for alignment diagnostics and visualization.

Define staircase plans

$$P_{ij}^{(a,b)} = \begin{cases} \exp(S_{ij} + u_i^{(a)} + v_j^{(b)}), & (i, j) \in \Omega, \\ 0, & (i, j) \notin \Omega. \end{cases}$$

Let \mathcal{L} be a scalar loss depending on $\tilde{O}^{[R]}$, let $G = \partial \mathcal{L} / \partial \tilde{O}^{[R]}$, and define

$$Z_{ij} = \langle G_i, V_j \rangle, \quad g_u = (P^{(R,R)} \odot Z) \mathbf{1}, \quad g_v = (P^{(R,R)} \odot Z)^\top \mathbf{1}.$$

Proposition 1 (Exact Fixed-Depth Tail Adjoint). *The cotangents of the refinement duals satisfy*

$$\bar{v}^{(R)} = g_v, \tag{3}$$

$$\bar{u}^{(R)} = g_u - P^{(R,R)} \bar{v}^{(R)}, \tag{4}$$

$$\bar{v}^{(t-1)} = -(P^{(t,t-1)})^\top \bar{u}^{(t)}, \quad t = R, R-1, \dots, 1, \tag{5}$$

$$\bar{u}^{(t-1)} = -P^{(t-1,t-1)} \bar{v}^{(t-1)}, \quad t = R, R-1, \dots, 2, \tag{6}$$

where the final line stops at $t = 2$ because the base state is stop-gradient. The score-space cotangent is

$$\bar{S} = P^{(R,R)} \odot Z - \sum_{t=1}^R \left[P^{(t,t)} \odot (\mathbf{1} \bar{v}^{(t)\top}) + P^{(t,t-1)} \odot (\bar{u}^{(t)} \mathbf{1}^\top) \right]. \tag{7}$$

For the reported TPU kernel we use $R = 2$, which yields the staircase

$$(P^{(2,2)}, P^{(2,1)}, P^{(1,1)}, P^{(1,0)}).$$

Proposition 2 (One-Reference-Tile $R = 2$ Backward Schedule). For any staircase pair $(a, b) \in \{(2, 2), (2, 1), (1, 1), (1, 0)\}$,

$$P^{(a,b)} = P^{(2,2)} \odot \exp(u^{(a)} - u^{(2)}) \odot \exp(v^{(b)} - v^{(2)}).$$

Define

$$\alpha_i = \exp(u_i^{(1)} - u_i^{(2)}), \quad \beta_j = \exp(v_j^{(1)} - v_j^{(2)}), \quad \delta_j = \exp(v_j^{(0)} - v_j^{(2)}).$$

Then on the active support the exact $R = 2$ score-space VJP is

$$\bar{S}_{ij} = P_{ij}^{(2,2)} \left[Z_{ij} - \bar{v}_j^{(2)} - \beta_j \bar{u}_i^{(2)} - \alpha_i \beta_j \bar{v}_j^{(1)} - \alpha_i \delta_j \bar{u}_i^{(1)} \right].$$

Hence, for a $B \times B$ score tile, the exact backward can be scheduled with one resident reference plan tile $P_{I,J}^{(2,2)}$, the corresponding $O(B)$ vector slices, and the $O(Bd)$ activation/cotangent slices needed to form $S_{I,J}$ and $Z_{I,J}$. The remaining staircase factors are never formed as resident plan tiles. For fixed block size, head dimension, band width, T , and $R = 2$, the schedule uses $O(Ld)$ input storage, $O(L)$ global vector state, and $O(LW)$ tile arithmetic for the tail backward.

Remark 2 (Centered gauge ledger). The displayed formula is the ungauged statement. If the stored centered representatives satisfy

$$\tilde{u}^{(t)} = u^{(t)} - c_t \mathbf{1}, \quad \tilde{v}^{(t)} = v^{(t)} + c_t \mathbf{1},$$

then same-time plans are unchanged but mixed-time plans are not. With

$$\tilde{\alpha}_i = \exp(\tilde{u}_i^{(1)} - \tilde{u}_i^{(2)}), \quad \tilde{\beta}_j = \exp(\tilde{v}_j^{(1)} - \tilde{v}_j^{(2)}), \quad \tilde{\delta}_j = \exp(\tilde{v}_j^{(0)} - \tilde{v}_j^{(2)}),$$

the ungauged mixed factors recovered from the centered ledger are

$$P_{ij}^{(2,1)} = e^{c_2 - c_1} P_{ij}^{(2,2)} \tilde{\beta}_j, \quad P_{ij}^{(1,1)} = P_{ij}^{(2,2)} \tilde{\alpha}_i \tilde{\beta}_j, \quad P_{ij}^{(1,0)} = e^{c_1 - c_0} P_{ij}^{(2,2)} \tilde{\alpha}_i \tilde{\delta}_j.$$

Appendix A records this explicitly because the mixed-time factors are not gauge-invariant.

For $R = 2$, equation (7) expands to

$$\begin{aligned} \bar{S} &= P^{(2,2)} \odot Z - P^{(2,2)} \odot (\mathbf{1} \bar{v}^{(2)\top}) - P^{(2,1)} \odot (\bar{u}^{(2)} \mathbf{1}^\top) \\ &\quad - P^{(1,1)} \odot (\mathbf{1} \bar{v}^{(1)\top}) - P^{(1,0)} \odot (\bar{u}^{(1)} \mathbf{1}^\top). \end{aligned} \quad (8)$$

The reconstruction identity above then replaces separate formation of the last three plan tiles with row and column rescalings of $P^{(2,2)}$.

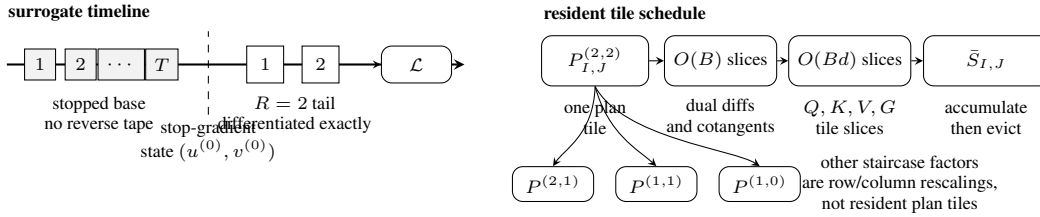


Figure 1: Stopped-base surrogate and $R = 2$ streaming backward schedule. Left: the T -step base solve provides a stop-gradient state and only the two tail refinements are differentiated. Right: each active score tile materializes one reference plan tile $P_{I,J}^{(2,2)}$, combines it with $O(B)$ vector slices and $O(Bd)$ activation/cotangent slices, accumulates the score cotangent, and evicts the tile; the remaining staircase factors are recovered by row/column rescaling.

Figure 1 summarizes the stop-gradient boundary and the tile-level memory schedule. The schedule is the signature implementation observation in the manuscript: it converts the explicit four-factor $R = 2$ backward into evaluation from one reference plan tile plus cheap row and column modifiers, which is why the method maps cleanly to streaming accelerator kernels.

Why $R = 2$. The multiplicative orbit identity itself is not unique to $R = 2$. Relative to any chosen base staircase plan, every other staircase plan factors by the corresponding dual differences in the same way. What is special about $R = 2$ is that the exact adjoint closes into the compact four-factor formula above, so the identity yields a concrete one-reference-tile schedule rather than a larger family of rescaled plans.

2.3 Single-Active-Dustbin Bridge

The current dustbin TPU path does not use a new OT solver. Instead, it augments the unit-target problem. Let the base sequence length be L and let $B = 128$ denote the dustbin block size used in the implementation. Define augmented tensors

$$\tilde{Q}, \tilde{K}, \tilde{V} \in \mathbb{R}^{(L+B) \times d}$$

by appending one learned dustbin token per side together with $B - 1$ inactive filler tokens. The masks are augmented analogously: one appended token is active, the rest are inactive fillers. The implementation then applies the same balanced tail-refinement solver to this augmented system, with effective band width

$$\tilde{W} = \max(W, L).$$

The current reported implementation is exactly the unit-target surrogate on the support induced by this widened generic band mask plus inactive-filler masks. A hypothetical sparse-spoke implementation would instead use

$$\tilde{\Omega} = \Omega_{\text{band}} \cup \{(i, d_k) : i \in I_q\} \cup \{(d_q, j) : j \in I_k\} \cup \{(d_q, d_k)\},$$

where d_q and d_k are the active appended dustbin row and column; that support would have $|\Omega_{\text{band}}| + O(L)$ active edges. The inactive fillers carry zero mask mass. Because the current reported code path realizes the bridge through the generic widened band mask $\tilde{W} = \max(W, L)$, its arithmetic should be accounted as $O(L\tilde{W})$, which becomes dense $O(L^2)$ when $W < L$. We do not claim the current dustbin path has the same long-context complexity as the balanced banded path in that regime.

Proposition 3 (Dustbin Augmentation Bridge). *Let $(\tilde{Q}, \tilde{K}, \tilde{V}, \tilde{\Omega})$ denote the dustbin-augmented tensors and active support constructed above. Then the current dustbin-block path is exactly the same unit-target fixed-support tail-refinement surrogate as in Section 2.2, but applied on the augmented state space.*

Corollary 1 (Exact $R = 2$ Adjoint on the Augmented State Space). *Apply Propositions 1 and 2 to the augmented system. Then the current dustbin-augmented transport path inherits the exact fixed-depth adjoint and the same one-reference-tile schedule on the augmented support.*

This is the first dustbin extension carried into the unified paper because it already matches the cloud path. It is a bridge theorem, not a departure from the central balanced factorization. With one active dustbin token per side, the dustbin marginal capacity is one unit on each side; arbitrary gap capacity would require enlarged dustbin marginals, multiple active dustbin tokens, or a genuinely unbalanced model.

2.4 A Local Surrogate-Bias Bound

The fixed-depth backward is exact for the surrogate it differentiates. A separate question is how far that surrogate gradient can be from the gradient through the full stopped-base computation. Let

$$z = (u, v), \quad \Phi_x(z) = z^+,$$

be the centered one-step refinement map at differentiable parameters x , and let $A_x(z)$ denote the transport application map. Write

$$z_T(x) = \Phi_x^T(z_0), \quad \Psi_x^R(z) = A_x(\Phi_x^R(z)).$$

Then the full fixed-depth gradient is

$$g_{\text{full}}^{T,R}(x) = \nabla_x \Psi_x^R(z_T(x)),$$

while the stop-gradient surrogate uses

$$g_{\text{surr}}^{T,R}(x) = \partial_x \Psi_x^R(z) \Big|_{z=z_T(x)}.$$

Theorem 1 (Local Surrogate-Bias Bound). *Assume fixed support, C^1 dependence of Φ_x and A_x on (x, z) , and constants $\rho \in [0, 1)$, $L_\Phi > 0$, and $L_A > 0$ such that*

$$\|D_z \Phi_x(z)\| \leq \rho, \quad \|D_x \Phi_x(z)\| \leq L_\Phi, \quad \|D_z A_x(z)\| \leq L_A$$

on a forward-invariant neighborhood. Then

$$g_{\text{full}}^{T,R}(x) - g_{\text{surr}}^{T,R}(x) = D_z \Psi_x^R(z_T(x)) D_x z_T(x),$$

and

$$\|g_{\text{full}}^{T,R}(x) - g_{\text{surr}}^{T,R}(x)\| \leq \frac{L_A L_\Phi}{1 - \rho} \rho^R.$$

The point of this bound is modest but useful: once the support is fixed and the refinement map is locally contractive, the stop-gradient bias decays geometrically in the tail depth R . We also record the finite-instance version used by the validation harness.

Proposition 4 (Projective Sinkhorn Contraction Certificate). *Consider a strictly positive active block of the balanced or dustbin-augmented support, and let*

$$K_{ij} = \exp(S_{ij})$$

be the positive kernel on that block, using the scaled score convention from Section 2.1. For positive column scalings c, c' , define the two-half-step Sinkhorn scaling map

$$\mathcal{T}(c) = b \circ [K^\top (a \circ (Kc))],$$

with positive marginals a, b ; in our normalized update $a = b = \mathbf{1}$. Let d_H denote Hilbert's projective metric on the positive cone and let $\Delta(A)$ be the projective diameter of a positive linear map A . Then

$$d_H(\mathcal{T}(c), \mathcal{T}(c')) \leq \rho_H d_H(c, c'), \quad \rho_H = \tanh\left(\frac{\Delta(K)}{4}\right) \tanh\left(\frac{\Delta(K^\top)}{4}\right) < 1.$$

Equivalently, in log scalings, with $\Phi_{\text{col}}(v) = \log \mathcal{T}(e^v)$ modulo additive gauge, the centered half-step pair is a contraction in oscillation seminorm:

$$\text{osc}(\Phi_{\text{col}}(v) - \Phi_{\text{col}}(v')) \leq \rho_H \text{osc}(v - v').$$

If $\Omega_S = \max_{(i,j)} S_{ij} - \min_{(i,j)} S_{ij}$ on the active block, then a computable sufficient bound is

$$\rho_H \leq \tanh^2\left(\frac{\Omega_S}{2}\right) < 1.$$

Equivalently, for unscaled logits \bar{S} with $S = \bar{S}/\varepsilon$, this reads

$$\rho_H \leq \tanh^2\left(\frac{\Omega_{\bar{S}}}{2\varepsilon}\right).$$

This proposition is a support-local certificate, not a claim about masked zeros. The Birkhoff–Hopf argument [Birkhoff, 1957, Bushell, 1973] applies on strictly positive active blocks after masked entries and inactive dustbin fillers have been excluded. The dustbin bridge preserves the statement because the active dustbin token is part of the augmented positive block, while the inactive filler tokens are outside the cone on which the contraction is asserted.

Proposition 5 (A Posteriori Bias Certificate). *Let $F_R(x, z)$ denote the scalar tail objective obtained by applying the terminal loss to $A_x(\Phi_x^R(z))$, and define the measured base-state cotangent*

$$\eta_R(x) = \nabla_z F_R(x, z) \Big|_{z=z_T(x)}.$$

Then the full-gradient remainder omitted by the stopped-base surrogate is exactly

$$\nabla_x F_R(x, z_T(x)) - \partial_x F_R(x, z) \Big|_{z=z_T(x)} = D_x z_T(x)^\top \eta_R(x).$$

Consequently, for any compatible norm,

$$\|\Delta g_R\| \leq \|D_x z_T(x)^\top\| \|\eta_R(x)\|.$$

This certificate is operational: η_R is the base cotangent produced by the same fixed-depth tail reverse pass before it is discarded by the stop-gradient rule, and $D_x z_T(x)^\top \eta_R$ is a single VJP through the base Sinkhorn solve.

Corollary 2 (Certified Tail-Depth Selection). *Fix a tolerance $\tau > 0$ and a maximum tail depth R_{\max} . For each $R \leq R_{\max}$, let*

$$c_R(x) = D_x z_T(x)^\top \eta_R(x).$$

Let $C(R)$ be any nondecreasing implementation cost over the candidate depths $\{0, \dots, R_{\max}\}$. If the implementation chooses the first R such that $\|c_R(x)\| \leq \tau$ and returns the stopped-base gradient at that depth, then the returned gradient differs from full BPTT through the same T -step base solve by at most τ . Moreover, this first feasible R solves the discrete certified optimization problem

$$\min_{0 \leq R \leq R_{\max}} C(R) \quad \text{subject to} \quad \|c_R(x)\| \leq \tau.$$

If an upper bound $C_T(x) \geq \|D_x z_T(x)^\top\|$ is available, the same guarantee and optimality statement hold with the sufficient constraint $C_T(x) \|\eta_R(x)\| \leq \tau$.

This turns tail-depth choice into a small certified resource-allocation problem rather than a purely heuristic hyperparameter. Instead of solving an adjoint linear system, one can either use a fixed depth such as $R = 2$ when the certificate has already been calibrated, or periodically run the certificate VJP to verify that the stopped-base omission remains below a chosen tolerance.

Proposition 6 (Transport-Orbit Calculus). *Consider any finite collection of transport plans $P^{(a,b)}$ generated from the same masked score tensor S and the same active support, including the plans used by the $R = 2$ staircase, the T stopped base reverse pass, the R differentiable tail reverse pass, and the certificate VJP $D_x z_T^\top \eta_R$. This fixed-score condition is essential: under an ε -scaling continuation schedule, the orbit statement applies stagewise to plans using the same effective score $S^{(s)} = \bar{S}/\varepsilon_s$, not across different temperature stages. Fix any reference plan $P^* = P^{(a_*, b_*)}$ in this collection and define*

$$r^{(a)} = \exp(u^{(a)} - u^{(a_*)}), \quad s^{(b)} = \exp(v^{(b)} - v^{(b_*)}).$$

Then every plan in the collection lies in the row/column scaling orbit of P^ :*

$$P^{(a,b)} = \text{diag}(r^{(a)}) P^* \text{diag}(s^{(b)}).$$

Equivalently, for any finite sum of plan-weighted score cotangent terms

$$G = \sum_{\ell=1}^m P^{(a_\ell, b_\ell)} \odot H_\ell,$$

one has the single-reference representation

$$G = P^* \odot \sum_{\ell=1}^m (r^{(a_\ell)} (s^{(b_\ell)})^\top) \odot H_\ell.$$

Consequently, for fixed T , R , band width W , and head dimension d , the stopped gradient, the certified omitted-gradient VJP, and the certified tail-depth test can all be evaluated blockwise with $O((T+R)LW)$ arithmetic, $O(Ld)$ input storage, and $O((T+R)L)$ vector state, while materializing only one transport tile at a time. The compiler abstraction is therefore not a special four-plan trick: it is accumulation over a single transport orbit.

3 Validation and Experiments

3.1 Exactness Validation of the Masked Surrogate

We first separate surrogate correctness from systems scale. On synthetic masked problems for which exact autodiff through the same centered surrogate remains tractable, we compare the optimized $R = 2$ kernel against a pure-JAX reference. Table 1 reports representative maximum absolute gradient deviations under the default validation setting: float32 arithmetic, $\varepsilon = 1$, no ε -scaling continuation, band width 256, $R = 2$, centered potentials, and masked inactive entries zeroed.

Length L	$\max \Delta Q $	$\max \Delta K $	$\max \Delta V $	Max rel. L_2
512	1.05×10^{-5}	1.73×10^{-6}	1.06×10^{-9}	5.78×10^{-2}
1024	5.70×10^{-6}	8.13×10^{-7}	2.55×10^{-10}	5.76×10^{-2}
2048	5.50×10^{-6}	9.17×10^{-7}	2.29×10^{-10}	5.05×10^{-2}

Table 1: Gradient deviations between the optimized masked $R = 2$ kernel and exact autodiff through the same centered surrogate. The final column is the worst relative L_2 error among $(\partial Q, \partial K, \partial V)$; the corresponding worst absolute L_2 errors are 6.59×10^{-5} , 4.11×10^{-5} , and 2.62×10^{-5} .

The table is primarily a kernel-equivalence check, not a full numerical-analysis study. The relative L_2 errors are largest for the small-norm Q gradients, whose reference L_2 norms are 1.14×10^{-3} , 7.14×10^{-4} , and 5.18×10^{-4} in the three rows; the absolute L_2 errors remain below 6.6×10^{-5} and the output relative L_2 errors are below 1.8×10^{-7} .

Additional forward-consistency checks run through lengths 512, 1024, 2048, 4096, 8192, and 16384, with extended spot checks at 32768, 65536, and 131072. We treat the larger checks as forward-consistency evidence rather than as exact-gradient checks.

To calibrate the local surrogate-bias discussion, we also compared tail-refinement gradients against full BPTT through the stopped-base solve on the same synthetic masked setup at $L = 512$, $d = 8$, $T = 15$, $W = 256$, and $\varepsilon = 1$. Over seeds 0, 1, 2, the worst-case gradient discrepancy $\max\{|\Delta Q|, |\Delta K|, |\Delta V|\}$ was 1.49×10^{-4} for $R = 0$, 1.63×10^{-5} for $R = 1$, 1.42×10^{-5} for $R = 2$, and 1.42×10^{-5} for $R = 4$. In this local exact-gradient calibration, the main empirical drop therefore occurs between zero tail refinement and the first one or two refinement steps, while $R = 2$ and $R = 4$ are already effectively tied at the scale of the masked validation harness.

Table 2 reports the a posteriori certificate from Proposition 5 on a smaller full-BPTT setting where the base-solve VJP can be checked directly ($L = 128$, $d = 8$, $T = 15$, $W = 128$, seeds 0, 1, 2). The certificate reconstructs the full-gradient remainder to numerical precision and shows rapid decay of the measured base-state cotangent.

Tail depth R	$\max \ \eta_R\ _2$	$\max \Delta g_R $	certificate residual
0	5.89×10^{-3}	6.29×10^{-4}	2.47×10^{-10}
1	5.40×10^{-4}	5.93×10^{-5}	3.64×10^{-11}
2	5.47×10^{-5}	5.33×10^{-6}	2.84×10^{-11}
4	9.03×10^{-7}	9.99×10^{-8}	2.74×10^{-11}

Table 2: A posteriori surrogate-bias certificate. The residual is the maximum absolute difference between the actual full-vs-stopped gradient gap and the certified base-solve VJP $D_x z_T^\top \eta_R$.

Using the certified selector from Corollary 2 with max-absolute tolerance 10^{-5} selects $R = 2$ on all three seeds in this calibration. Since the per-depth tail cost is monotone in R , this is the cheapest certified depth among the tested candidates and gives a certificate-level justification for using $R = 2$ as the reported TPU depth.

We also validate the transport-orbit calculus from Proposition 6 directly over all $2(T + R)$ base and tail half-step plans at $T = 15$, $R = 2$, $L = 128$. Reconstructing every plan from the final reference plan gives maximum log-domain reconstruction error 1.91×10^{-6} . Appendix C reports two additional diagnostics. The controlled direct-four-plan score-adjoint diagnostic reduces logical active plan-factor storage by exactly $4\times$ and gives $1.29\text{--}2.20\times$ post-compilation CPU speedups with maximum score-cotangent discrepancy at most 4.77×10^{-7} ; it is still a dense-JAX CPU materialization check, not a production TPU kernel benchmark. The same appendix also reports projective contraction certificates computed from the promoted Pfam checkpoint.

3.2 Short Pfam Screen on TPU v6e-8

The first empirical bridge is the short Pfam screen on TPU v6e-8. All four core configurations complete end-to-end:

k2_eps1, k4_eps1, muot_dustbin_mono, muot_dustbin_hybrid.

Each uses 50,000 training pairs, $T = 15$ base iterations, band width 1024, and global batch size 64. Table 3 reports the step-50 screen snapshot.

Config	Step 50 Loss	Step 50 CE	Step 50 Mono	Throughput (ex/s)
k2_eps1	3.5778	5.3223	0.3353	8.46
k4_eps1	3.5779	5.3223	0.3353	8.38
muot_dustbin_mono	3.9030	5.3258	0.4155	8.41
muot_dustbin_hybrid	4.6250	5.3244	0.4162	8.45

Table 3: Short TPU v6e-8 Pfam screen across the four core balanced and dustbin-augmented configurations.

Two immediate conclusions follow. First, on the balanced path we observe no meaningful difference between $R = 2$ and $R = 4$ at this short-screen budget, while $R = 2$ remains slightly faster; this is a short smoke screen rather than evidence that the runs have fully converged. Second, the single-active-dustbin bridge is operational in the same TPU training harness, with the widened-support cost caveat from Section 2.4.

3.3 Promoted Balanced Run

We then promoted the balanced k2_eps1 configuration to the longer-budget TPU training path. The full objective details are given in the protocol notes in the appendix; for the interpretation of the main text, the important point is that this promotion is a trainability and systems-stability test of the factorization-backed balanced $R = 2$ path. The run reached step 1437, repeatedly persisted checkpoints at steps 250, 500, 750, 1000, and 1250, and sustained approximately 8.5 examples per second after startup warmup. The initial throughput at step 0 was 2.67 examples per second, after which the run stabilized near 8.5 examples per second for the remainder of the budget.

Checkpoint / reference	Rec.	Sparse CE	Bary. MAE	Bary. ≤ 5	Mono.
Step 0	5.5730	5.5335	65.1369	0.0406	0.4309
Step 1437	2.0539	5.3046	64.5921	0.0403	0.5003
Diag. ref. (step-0 V)	5.6320	17.8155	1.6367	0.9372	0.0000
Diag. ref. (step-1437 V)	2.0142	17.8155	1.6367	0.9372	0.0000

Table 4: Held-out Pfam test-shard evaluation on 100 examples. “Bary.” reports row-normalized transport-barycenter error against supervised target columns. The diagonal references use a length-scaled monotone point-mass alignment; their sparse CE uses a 10^{-12} off-diagonal floor and is not directly comparable to the soft Sinkhorn CE.

Example-bootstrap 95% intervals are [5.03, 6.06] and [1.78, 2.30] for reconstruction at steps 0 and 1437, and [5.49, 5.58] and [5.26, 5.35] for sparse CE. For the step-1437 diagonal reference, the intervals are [1.73, 2.31] for reconstruction, [1.33, 1.96] for barycenter MAE, and [0.90, 0.97] for barycenter within five columns. An untrained same-projection flash-attention reference gives reconstruction 5.5753 and sparse CE 5.5383, matching the step-0 Sinkhorn checkpoint; this is an initialization sanity reference, not a trained baseline. The promoted run is therefore evidence of stability, checkpointability, and reconstruction improvement for the factorization-backed path. The CE change is diagnostic, target-barycenter alignment metrics do not materially improve, barycenter-within-five and monotonicity do not improve, and the diagonal reference remains much stronger on alignment metrics. This experiment therefore does not establish an alignment-task advantage.

4 Discussion and Conclusion

The contribution is exact fixed-depth backward theory for a balanced fixed-support surrogate, with a single-active-dustbin unit-target bridge, centered-kernel validation, and scoped TPU trainability evidence. It is not a full KL-unbalanced gap model, a global masked-support guarantee, a FlashSinkhorn/direct-adjoint timing comparison, a trained-baseline comparison, or a CE-optimized alignment result; these remain separate tests of systems efficiency and task value.

References

- Shaojie Bai, J Zico Kolter, and Vladlen Koltun. Deep equilibrium models. In *Advances in Neural Information Processing Systems*, volume 32, 2019.
- Iz Beltagy, Matthew E. Peters, and Arman Cohan. Longformer: The long-document transformer. *arXiv preprint arXiv:2004.05150*, 2020. doi: 10.48550/arXiv.2004.05150.
- Garrett Birkhoff. Extensions of Jentzsch’s theorem. *Transactions of the American Mathematical Society*, 85(1):219–227, 1957. doi: 10.1090/S0002-9947-1957-0087058-6.
- P. J. Bushell. Hilbert’s metric and positive contraction mappings in a Banach space. *Archive for Rational Mechanics and Analysis*, 52(4):330–338, 1973. doi: 10.1007/BF00247467.
- Marco Cuturi. Sinkhorn distances: Lightspeed computation of optimal transport. In *Advances in Neural Information Processing Systems*, volume 26, 2013.
- Zeming Lin, Halil Akin, Roshan Rao, Brian Hie, Zhongkai Zhu, Wenting Lu, Nikita Smetanin, Robert Verkuil, Ori Kabeli, Yaniv Shmueli, et al. Evolutionary-scale prediction of atomic-level protein structure with a language model. *Science*, 379(6637):1123–1130, 2023. doi: 10.1126/science.ade2574.
- Giulia Luise, Alessandro Rudi, Massimiliano Pontil, and Carlo Ciliberto. Differential properties of Sinkhorn approximation for learning with Wasserstein distance. In *Advances in Neural Information Processing Systems*, volume 31, 2018.
- Jaina Mistry, Sara Chuguransky, Lowri Williams, Matloob Qureshi, Gustavo A Salazar, et al. Pfam: The protein families database in 2021. *Nucleic Acids Research*, 49(D1):D412–D419, 2021. doi: 10.1093/nar/gkaa913.
- Gabriel Peyré and Marco Cuturi. Computational optimal transport: With applications to data science. *Foundations and Trends in Machine Learning*, 11(5-6):355–607, 2019. doi: 10.1561/22000000073.
- Temple F Smith and Michael S Waterman. Identification of common molecular subsequences. *Journal of Molecular Biology*, 147(1):195–197, 1981. doi: 10.1016/0022-2836(81)90087-5.
- Felix X.-F. Ye, Xingjie Li, An Yu, Ming-Ching Chang, Linsong Chu, and Davis Wertheimer. FlashSinkhorn: IO-aware entropic optimal transport. *arXiv preprint arXiv:2602.03067*, 2026. doi: 10.48550/arXiv.2602.03067.
- Manzil Zaheer, Guru Guruganesh, Kumar Avinava Dubey, Joshua Ainslie, Chris Alberti, Santiago Ontañón, Philip Pham, Anirudh Ravula, Qifan Wang, Li Yang, and Amr Ahmed. Big Bird: Transformers for longer sequences. In *Advances in Neural Information Processing Systems*, volume 33, pages 17283–17297, 2020.

A Balanced Tail-Refinement Proofs

Notation. For the appendix proofs we work with ungauged representatives satisfying the raw masked logsumexp half-step equations. Let Ω denote the active support and define

$$P_{ij}^{(a,b)} = \begin{cases} \exp(S_{ij} + u_i^{(a)} + v_j^{(b)}), & (i, j) \in \Omega, \\ 0, & (i, j) \notin \Omega. \end{cases}$$

$$u_i^{(t+1)} = -\log \left[\sum_{j:(i,j) \in \Omega} \exp(S_{ij} + v_j^{(t)}) \right], \quad (9)$$

$$v_j^{(t+1)} = -\log \left[\sum_{i:(i,j) \in \Omega} \exp(S_{ij} + u_i^{(t+1)}) \right]. \quad (10)$$

Centering map. Let $\mathbf{1}_q$ and $\mathbf{1}_k$ denote the all-ones vectors on valid queries and keys, and let

$$m = \frac{\mathbf{1}_q}{\mathbf{1}_q^\top \mathbf{1}_q}.$$

The implementation stores centered representatives via

$$\mathcal{C}(u, v) = (u - (m^\top u) \mathbf{1}_q, v + (m^\top u) \mathbf{1}_k).$$

Lemma 1 (Centering Pullback). *If (\bar{u}, \bar{v}) are cotangents on the outputs of \mathcal{C} , then*

$$\mathcal{C}^*(\bar{u}, \bar{v}) = (\bar{u} + m(\mathbf{1}_k^\top \bar{v} - \mathbf{1}_q^\top \bar{u}), \bar{v}).$$

Proof. Write $s = m^\top u$, so $\delta s = m^\top \delta u$. Then

$$\delta \mathcal{C}(u, v) = (\delta u - (\delta s) \mathbf{1}_q, \delta v + (\delta s) \mathbf{1}_k).$$

Pairing this variation with (\bar{u}, \bar{v}) and collecting coefficients of δu and δv yields the stated pullback. \square

Lemma 2 (Gauge Equivariance). *Let $\Gamma_c(u, v) = (u - c \mathbf{1}_q, v + c \mathbf{1}_k)$. Then the raw two-half-step map defined by equations (9)–(10) is gauge equivariant.*

Proof. Adding c to every valid key potential shifts every logsumexp argument in the u -update by the same constant, so the update subtracts c from every valid query potential. The v -update is identical with rows and columns swapped. \square

Proposition 7 (Centered Gauge Ledger). *Let $(\hat{u}^{(t)}, \hat{v}^{(t)})$ be the ungauged iterates and $(u^{(t)}, v^{(t)})$ the iterates produced by the centered implementation, both started from the same centered base pair. Then for every $t \geq 1$ there exists a scalar c_t such that*

$$(u^{(t)}, v^{(t)}) = \Gamma_{c_t}(\hat{u}^{(t)}, \hat{v}^{(t)}).$$

Consequently same-time plans are gauge-invariant,

$$\exp(S_{ij} + u_i^{(t)} + v_j^{(t)}) = \exp(S_{ij} + \hat{u}_i^{(t)} + \hat{v}_j^{(t)}),$$

but mixed-time staircase plans carry scalar gauge factors:

$$P_{\text{cent } ij}^{(a,b)} = e^{c_b - c_a} P_{\text{ung } ij}^{(a,b)}.$$

Equivalently,

$$P_{\text{ung } ij}^{(a,b)} = e^{c_a - c_b} P_{\text{cent } ij}^{(a,b)}.$$

The mixed factors are therefore not gauge-invariant unless $a = b$ or $c_a = c_b$.

Proof. The existence of c_t holds at $t = 1$ by definition of the centering step. Inductively, if the two previous representatives differ by a gauge transform, then gauge equivariance of the raw refinement step shows that the next raw outputs also differ by a gauge transform; applying \mathcal{C} merely chooses another representative of the same orbit. The same-time identity follows because the two gauge shifts cancel inside $u_i^{(t)} + v_j^{(t)}$. For mixed times,

$$u_i^{(a)} + v_j^{(b)} = \widehat{u}_i^{(a)} + \widehat{v}_j^{(b)} - c_a + c_b,$$

which gives the scalar factor. \square

Lemma 3 (When Centering Pullbacks Vanish). *For cotangents (\bar{u}, \bar{v}) on the outputs of \mathcal{C} , if*

$$\mathbf{1}_q^\top \bar{u} = \mathbf{1}_k^\top \bar{v},$$

then $\mathcal{C}^(\bar{u}, \bar{v}) = (\bar{u}, \bar{v})$. In the unit-target tail reverse pass, this equal-total condition holds at every full-step centering boundary.*

Proof. The first claim is immediate from the displayed formula for \mathcal{C}^* . For the tail reverse pass, the terminal transport application gives

$$\mathbf{1}_q^\top g_u = \sum_{ij} P_{ij}^{(R,R)} Z_{ij} = \mathbf{1}_k^\top g_v,$$

so the final centering pullback contributes no extra term. After pulling $\bar{v}^{(t)}$ through a same-time v -half-step, the same-time plan has unit column sums, hence

$$\mathbf{1}_q^\top \left[-P^{(t,t)} \bar{v}^{(t)} \right] = -\mathbf{1}_k^\top \bar{v}^{(t)}.$$

The resulting $\bar{u}^{(t)}$ has zero total once the direct terminal contribution has been combined at $t = R$, and thereafter the invariant is zero total on both components. Pulling a zero-total $\bar{u}^{(t)}$ through a unit-row-normalized u -half-step gives a zero-total $\bar{v}^{(t-1)}$. Thus each later centering boundary sees equal totals, so the explicit \mathcal{C}^* correction vanishes in the unit-target proof. If non-unit marginals are introduced, the corresponding normalized conditional kernels must be used in this invariant. \square

Lemma 4 (Half-Step Jacobians). *For every refinement step $t \geq 1$,*

$$\frac{\partial u_i^{(t)}}{\partial v_j^{(t-1)}} = -P_{ij}^{(t,t-1)}, \quad (11)$$

$$\frac{\partial v_j^{(t)}}{\partial u_i^{(t)}} = -P_{ij}^{(t,t)}. \quad (12)$$

Proof. Differentiate the masked logsumexp updates. For example,

$$\frac{\partial u_i^{(t)}}{\partial v_j^{(t-1)}} = -\frac{\exp(S_{ij} + v_j^{(t-1)})}{\sum_{k:(i,k) \in \Omega} \exp(S_{ik} + v_k^{(t-1)})} = -\exp(S_{ij} + u_i^{(t)} + v_j^{(t-1)}) = -P_{ij}^{(t,t-1)}.$$

The second identity is identical with rows and columns swapped. \square

Proof of Proposition 1.

Proof. By the preceding centering-pullback lemma, the explicit \mathcal{C}^* correction terms vanish at the full-step centering boundaries for the unit-target tail reverse pass. It therefore suffices to write the reverse equations for the raw half-steps, with the centered gauge ledger applied separately when translating mixed-time factors between representatives. The direct terminal transport application contributes $P^{(R,R)} \odot Z$ to \bar{S} together with

$$\bar{v}^{(R)} = g_v, \quad \bar{u}_{\text{direct}}^{(R)} = g_u.$$

Before moving to the preceding u -half-step, this terminal $\bar{v}^{(R)}$ must be pulled through the final $v^{(R)}$ update. This contributes

$$\bar{S} \text{--} = P^{(R,R)} \odot (\mathbf{1}\bar{v}^{(R)\top}), \quad \bar{u}^{(R)} = \bar{u}_{\text{direct}}^{(R)} - P^{(R,R)}\bar{v}^{(R)}.$$

Now fix a reverse step $t \in \{1, \dots, R\}$. Pulling $\bar{u}^{(t)}$ back through the u -half-step uses the Jacobian $-P^{(t,t-1)}$:

$$\bar{v}^{(t-1)} = -(P^{(t,t-1)})^\top \bar{u}^{(t)}, \quad \bar{S} \text{--} = P^{(t,t-1)} \odot (\bar{u}^{(t)} \mathbf{1}^\top).$$

For $t \geq 2$, pulling $\bar{v}^{(t-1)}$ back through the v -half-step uses the Jacobian $-P^{(t-1,t-1)}$:

$$\bar{u}^{(t-1)} = -P^{(t-1,t-1)}\bar{v}^{(t-1)}, \quad \bar{S} \text{--} = P^{(t-1,t-1)} \odot (\mathbf{1}\bar{v}^{(t-1)\top}).$$

For $t = 1$, the u -half-step pullback produces the stopped-base cotangent $\bar{v}^{(0)}$ and the final mixed-time score term $P^{(1,0)} \odot (\bar{u}^{(1)} \mathbf{1}^\top)$. No earlier v -half-step is pulled back inside the differentiable tail because the base pair is stopped. Summing the direct terminal term with the reverse-time half-step contributions yields equation (7). \square

Proof of Proposition 2.

Proof. For any two staircase plans,

$$\frac{P_{ij}^{(a,b)}}{P_{ij}^{(2,2)}} = \exp(u_i^{(a)} - u_i^{(2)} + v_j^{(b)} - v_j^{(2)}),$$

which gives the exact reconstruction formula immediately. For the three non-reference factors in the $R = 2$ staircase this gives

$$P_{ij}^{(2,1)} = P_{ij}^{(2,2)} \beta_j, \quad P_{ij}^{(1,1)} = P_{ij}^{(2,2)} \alpha_i \beta_j, \quad P_{ij}^{(1,0)} = P_{ij}^{(2,2)} \alpha_i \delta_j.$$

Substituting these three identities into the expanded VJP in equation (8) and factoring out $P_{ij}^{(2,2)}$ gives

$$\bar{S}_{ij} = P_{ij}^{(2,2)} \left[Z_{ij} - \bar{v}_j^{(2)} - \beta_j \bar{u}_i^{(2)} - \alpha_i \beta_j \bar{v}_j^{(1)} - \alpha_i \delta_j \bar{u}_i^{(1)} \right].$$

Thus every entry of the direct four-factor adjoint is reproduced exactly from the reference plan and vector modifiers.

For a tile $I \times J$, compute $P_{I,J}^{(2,2)}$ once from $S_{I,J}$, $u_I^{(2)}$, and $v_J^{(2)}$, compute $Z_{I,J}$ from the resident slices of G_I and V_J , and form the bracketed modifier using only the slices of α_I , $\bar{u}_I^{(2)}$, $\alpha_I \bar{u}_I^{(1)}$, β_J , δ_J , $\bar{v}_J^{(2)}$, and $\beta_J \bar{v}_J^{(1)}$. Multiplying the single resident reference tile by this modifier yields the exact score-space VJP tile. The value-gradient term uses the same resident reference plan tile, since $\partial \mathcal{L} / \partial V$ receives $(P_{I,J}^{(2,2)})^\top G_I$. All subsequent propagation to Q and K is linear in the score cotangent tile, so it can be accumulated before the tile is evicted. The stated storage and arithmetic bounds follow by streaming over the $O(LW/B^2)$ active tiles with fixed B , d , W , and fixed tail depth. \square

B Proofs for the Dustbin Bridge and Surrogate Bias

Proof of Proposition 3.

Proof. After constructing the augmented tensors and masks, the implementation calls the same unit-target Sinkhorn forward and backward path as in Section 2.2. Because only the first appended token in each dustbin block is active, every transport entry touching the remaining fillers is identically zero. Because the effective band width is $\widetilde{W} = \max(W, L)$, every active base token can reach the active dustbin token on the opposite side, and conversely the active dustbin query can reach every active base key. Thus the implemented path is exactly the unit-target fixed-support surrogate on an enlarged state space. The proposition is an algebraic code-path statement; the cost of the current widened-band realization is governed by \widetilde{W} , as stated in Section 2.4. \square

Proof of Corollary 1.

Proof. Apply Propositions 1 and 2 to the augmented tensors and support from Proposition 3. No new algebra is introduced after the augmentation itself. \square

Proof of Theorem 1.

Proof. By the chain rule,

$$\nabla_x \Psi_x^R(z_T(x)) = \partial_x \Psi_x^R(z) \Big|_{z=z_T(x)} + D_z \Psi_x^R(z_T(x)) D_x z_T(x),$$

which gives the exact bias identity after subtracting the partial derivative term.

Next,

$$D_z \Psi_x^R(z_T(x)) = D_z A_x(z_{T+R}(x)) \prod_{r=0}^{R-1} D_z \Phi_x(z_{T+r}(x)),$$

so

$$\|D_z \Psi_x^R(z_T(x))\| \leq L_A \rho^R.$$

Differentiate the base recursion $z_{t+1}(x) = \Phi_x(z_t(x))$:

$$D_x z_{t+1}(x) = D_x \Phi_x(z_t(x)) + D_z \Phi_x(z_t(x)) D_x z_t(x).$$

Because z_0 is independent of x , repeated application of the norm bounds yields

$$\|D_x z_T(x)\| \leq L_\Phi \sum_{j=0}^{T-1} \rho^j \leq \frac{L_\Phi}{1-\rho}.$$

Combining the two estimates with the exact bias identity gives

$$\|g_{\text{full}}^{T,R}(x) - g_{\text{surr}}^{T,R}(x)\| \leq \frac{L_A L_\Phi}{1-\rho} \rho^R. \quad \square$$

Proof of Proposition 4.

Proof. Hilbert's projective metric on the positive cone is

$$d_H(x, y) = \log \frac{\max_i x_i / y_i}{\min_i x_i / y_i}.$$

Positive diagonal scaling and coordinatewise inversion preserve this metric: diagonal scaling cancels in the coordinate ratios, and inversion swaps the maximum and minimum ratios. By the Birkhoff–Hopf theorem, any positive linear map A with finite projective diameter $\Delta(A)$ satisfies

$$d_H(Ax, Ay) \leq \tanh\left(\frac{\Delta(A)}{4}\right) d_H(x, y).$$

Decompose the two-half-step map as

$$c \mapsto Kc \mapsto a \otimes (Kc) \mapsto K^\top(a \otimes (Kc)) \mapsto b \otimes K^\top(a \otimes (Kc)).$$

The two linear maps contribute Birkhoff–Hopf contraction factors $\tanh(\Delta(K)/4)$ and $\tanh(\Delta(K^\top)/4)$, while the marginal scalings and inversions are projective isometries. Therefore

$$d_H(\mathcal{T}(c), \mathcal{T}(c')) \leq \tanh\left(\frac{\Delta(K)}{4}\right) \tanh\left(\frac{\Delta(K^\top)}{4}\right) d_H(c, c').$$

Strict positivity on the active block gives finite projective diameters, hence $\rho_H < 1$.

For log scalings,

$$d_H(e^v, e^{v'}) = \text{osc}(v - v'), \quad \text{osc}(w) = \max_i w_i - \min_i w_i,$$

and additive centering does not change oscillation. This gives the log-potential contraction.

Finally, for a positive matrix $K_{ij} = \exp(S_{ij})$,

$$\Delta(K) = \log \max_{i,i',j,j'} \frac{K_{ij}K_{i'j'}}{K_{ij'}K_{i'j}} = \max_{i,i',j,j'} (S_{ij} + S_{i'j'} - S_{ij'} - S_{i'j}).$$

If $\Omega_S = \max S - \min S$ on the active block, the last expression is at most $2\Omega_S$. The same bound holds for K^\top . Substituting into the Birkhoff–Hopf coefficient yields

$$\rho_H \leq \tanh^2\left(\frac{\Omega_S}{2}\right),$$

and the unscaled-logit form follows from $S = \bar{S}/\varepsilon$. \square

Proof of Proposition 5.

Proof. By definition,

$$g_{\text{full}}(x) = \nabla_x F_R(x, z_T(x)), \quad g_{\text{surr}}(x) = \partial_x F_R(x, z)|_{z=z_T(x)}.$$

Applying the chain rule to the first expression gives

$$\nabla_x F_R(x, z_T(x)) = \partial_x F_R(x, z)|_{z=z_T(x)} + D_x z_T(x)^\top \nabla_z F_R(x, z)|_{z=z_T(x)}.$$

Subtracting the stopped-base partial derivative gives the identity with $\eta_R = \nabla_z F_R(x, z_T(x))$. The norm bound follows immediately from submultiplicativity for the chosen compatible operator norm. \square

Proof of Corollary 2.

Proof. Proposition 5 gives the exact identity $\Delta g_R = c_R(x)$. Therefore $\|c_R(x)\| \leq \tau$ implies $\|\Delta g_R\| \leq \tau$. If only an operator-norm bound $C_T(x) \geq \|D_x z_T(x)^\top\|$ is used, the bound in Proposition 5 gives

$$\|\Delta g_R\| \leq \|D_x z_T(x)^\top\| \|\eta_R(x)\| \leq C_T(x) \|\eta_R(x)\| \leq \tau.$$

For the optimization claim, let R^* be the first feasible depth. Every smaller depth is infeasible by definition of R^* , and every larger feasible depth has cost at least $C(R^*)$ because C is nondecreasing. Hence R^* minimizes $C(R)$ over the certified feasible set. \square

Proof of Proposition 6.

Proof. All plans in the collection use the same masked score tensor S and the same active support. If an ε -scaling schedule is used, this proof applies separately inside each fixed-temperature stage after replacing S by $S^{(s)} = \bar{S}/\varepsilon_s$; plans from different stages are not generally in one common row/column scaling orbit. For any two dual pairs on that support,

$$\frac{P_{ij}^{(a,b)}}{P_{ij}^{(a_*,b_*)}} = \exp(u_i^{(a)} - u_i^{(a_*)} + v_j^{(b)} - v_j^{(b_*)}),$$

which gives the orbit formula entrywise. Multiplying this identity by H_ℓ and summing over ℓ gives the single-reference representation for G . The reverse recurrences in Propositions 1 and 5 require only products of these plans with row or column cotangent vectors and score-space outer factors, all of which are instances of this representation. Each such product can therefore be evaluated by streaming one reference plan tile and applying the appropriate row and column multipliers. With fixed T , R , W , and d , each half-step contributes $O(LW)$ arithmetic and $O(L)$ vector state, while the input activations require $O(Ld)$ storage. \square

C Experimental Protocol Notes

The current manuscript uses three empirical layers:

1. exactness checks against exact autodiff on small masked problems;
2. a four-configuration TPU v6e-8 Pfam screen across balanced and dustbin-augmented paths;
3. a promoted long-budget balanced run for the factorization-backed $R = 2$ path, plus held-out checkpoint and deterministic diagonal-reference evaluation.

All TPU results use a single Cloud TPU v6e-8 host. The short screen uses 50,000 Pfam training pairs with the reported benchmark stack, and the promoted run uses the same benchmark family at longer budget. The biological inputs and language-model-derived embeddings are pre-existing assets rather than new data collection.

For the promoted balanced run, the objective weights were

$$\lambda_{\text{rec}} = 1, \quad \lambda_{\text{ce}} = 0, \quad \lambda_{\text{mono}} = 0,$$

so reconstruction loss was optimized directly while CE and monotonicity were logged diagnostically. Here reconstruction is the mean supervised value-vector MSE: for each active annotated query row i with target column c_i , we compare the transport output $\sum_j P_{ij} V_j$ to V_{c_i} , sum squared error over embedding dimensions, and average over active rows and heads. The anonymized supplementary code bundle contains the single-file balanced and dustbin-augmented transport kernel analyzed by the theory, a Sinkhorn-only Pfam training harness whose defaults match the reported v6e-8 promoted-run settings, the held-out checkpoint evaluator, the exactness-summary JSON used for Table 1, and the held-out metric JSON summaries used for Table 4. It intentionally omits cloud launchers, project-specific storage paths, checkpoints, logs, FlashAttention/FlashSinkhorn training branches, comparison adapters, measured TPU direct-adjoint outputs, and external data or embedding generation. The deterministic diagonal reference maps each active query ordinal to the corresponding length-scaled active key ordinal and uses the same value projection as the selected checkpoint. The reported empirical runs additionally depend on precomputed Pfam/ESM-2 shards and TPU environment setup, so the empirical claims are scoped to the disclosed protocol notes and reported artifacts rather than to a complete public data pipeline.

For the repository version used to prepare the manuscript, the synthetic diagnostics are reproduced with the JAX environment active by running `python scripts/validate_tail_refinement.py`, `python scripts/validate_orbit_factorization.py`, `python scripts/validate_tail_bias_certificate.py`, and `python scripts/benchmark_four_plan_adjoint.py`. These commands cover the synthetic exactness, orbit, bias-certificate, and local four-plan diagnostics; they do not reproduce the cloud TPU training run without the omitted external shards and environment setup. The supplementary code also includes `benchmark_production_backward_modes.py`, a TPU-facing harness that times the optimized tail-refinement backward and, at smaller feasible sizes, compares gradients against the exact-autodiff reference mode exposed by the same public Sinkhorn API. Its optional score-adjoint mode also isolates the block-sparse $R = 2$ score-cotangent stage and compares explicit stored-coordinate four-plan block materialization with the one-reference formula used by the centered implementation; this is scoped to that stage and is not a complete direct custom-VJP implementation or an ungauged gauge-recovered comparison. We include the harness to make the missing production measurement concrete, but we do not report it as an experimental result because the required TPU run was not completed.

The main external assets used in the experiments are public Pfam family data [Mistry et al., 2021] and ESM-2 embeddings from the public ESM-2 checkpoint [Lin et al., 2023]. Pfam is distributed under CC0 through the Pfam/InterPro documentation, and the `esm2_t6_8M_UR50D` weights used for the embeddings are distributed under the MIT license.

The present cloud-aligned dustbin path is the single-active-dustbin augmented unit-target surrogate. Genuinely KL-unbalanced transport, larger dustbin capacities, sparse-spoke dustbin supports, and differentiable support geometry remain natural follow-on directions, but they are not needed for the main claim carried by this manuscript.

Synthetic diagnostic visual summary. Figure 2 visualizes the exactness and bias-certificate summaries reported in Tables 1 and 2. The left panel is generated from the exactness-summary JSON included in the supplementary bundle. The right panel plots the a posteriori bias-certificate rows from Table 2; the selector tolerance line is the 10^{-5} criterion used to choose $R = 2$ in the local calibration.

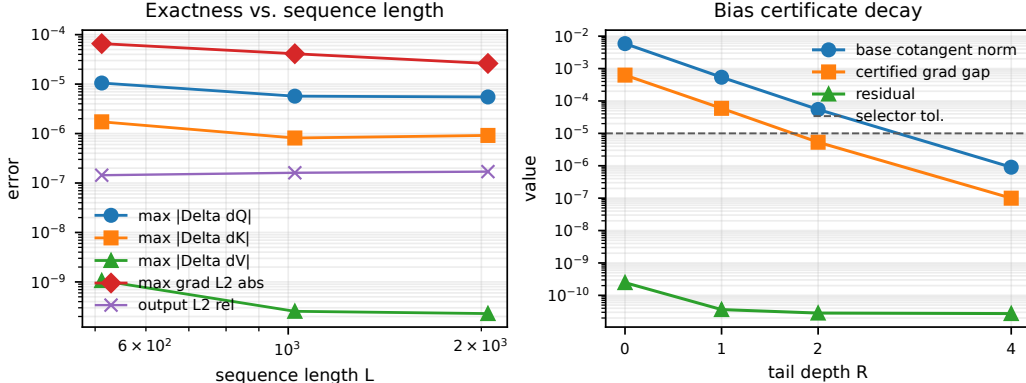


Figure 2: Synthetic tail-refinement diagnostics. Left: optimized $R = 2$ kernel deviations against exact autodiff through the same centered surrogate. Right: a posteriori bias-certificate decay with tail depth.

Qualitative checkpoint output on real Pfam inputs. Figure 3 visualizes a real Pfam/ESM-2 pair generated by the shard pipeline and evaluated with the saved step-0 and step-1437 Sinkhorn checkpoints. The selected pair has 223 query positions, 212 key positions, and 211 supervised alignment targets. For this example, the promoted checkpoint lowers reconstruction MSE from 4.86 to 1.61 and sparse CE from 5.40 to 5.19. The visualization is qualitative: it shows what the saved final checkpoint outputs on real inputs, while the aggregate held-out metrics remain those in Table 4.

Multiple qualitative checkpoint examples. Figure 4 repeats the final-checkpoint transport visualization for four local Pfam/ESM-2 candidates selected by reconstruction-MSE improvement from the first 36 scanned held-out shard examples, subject to at least 180 active targets and maximum visual length 320. The examples have 211–222 supervised targets and improve reconstruction MSE from 4.72–4.86 at step 0 to 1.52–1.61 at step 1437. This figure is a qualitative stress check of the saved checkpoint on multiple real inputs, not an additional benchmark; Table 4 remains the aggregate held-out summary.

Direct four-plan adjoint diagnostic. Table 5 isolates the $R = 2$ score-adjoint stage after the base and tail potentials are already available. The direct baseline forms the four staircase factors ($P^{(2,2)}, P^{(2,1)}, P^{(1,1)}, P^{(1,0)}$) separately; the one-reference implementation forms only $P^{(2,2)}$ and applies the row/column modifiers from Proposition 2. This is a local dense-JAX CPU diagnostic rather than a TPU systems benchmark, so it should be read as a controlled materialization check, not as a FlashSinkhorn comparison or a production wall-clock claim.

L	W	Direct ms	One-ref ms	Speedup	Max $ \Delta \bar{S} $
512	256	2.32	1.06	2.20×	4.77×10^{-7}
1024	256	7.01	5.44	1.29×	1.19×10^{-7}
2048	256	60.51	39.58	1.53×	2.38×10^{-7}

Table 5: Controlled score-adjoint benchmark for direct four-plan materialization versus the one-reference representation. Logical active plan-factor storage is reduced by exactly $4\times$ in all rows: 3.15/0.79 MB, 7.35/1.84 MB, and 15.76/3.94 MB for direct/one-reference respectively. Timings are mean post-compilation CPU times over 20 repetitions.

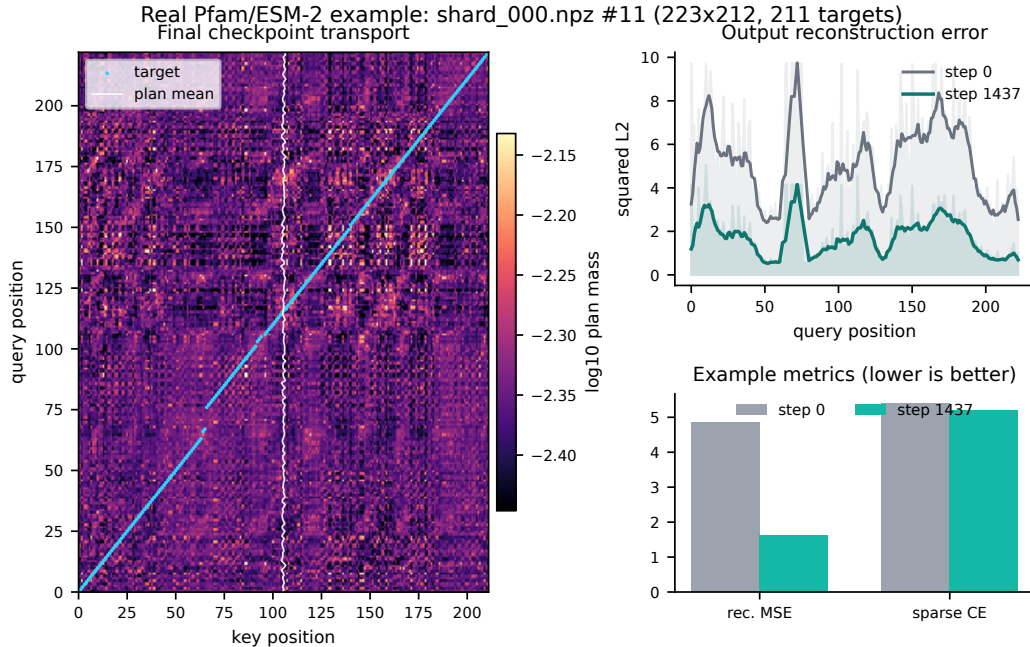


Figure 3: Qualitative model output on a real Pfam/ESM-2 pair. Left: final-checkpoint tail-refinement transport plan, with supervised target columns in cyan and the plan barycenter in white. Right: per-position output reconstruction error and example-level lower-is-better metrics before and after promotion.

Analytic memory ledger. The production benchmark request ultimately needs measured TPU HBM and wall-clock numbers, which Table 5 does not provide. To make the memory claim concrete, Table 6 gives an analytic ledger for the balanced $R = 2$ path at the reported long-context setting $L = 16384$, half-band width $W = 1024$, block size $B = 128$, head dimension $d = 64$, and float32 storage. The ledger compares storage inside the $R = 2$ adjoint only; it is not a measured comparison against FlashAttention or FlashSinkhorn workspaces. The command `python scripts/estimate_r2_backward_memory.py` reproduces these values.

Quantity	Direct four-plan	One-reference
Active support entries per head		32.52M
Logical materialized plan factors	496.23 MiB	124.06 MiB
Resident plan tile at $B = 128$	0.2500 MiB	0.0625 MiB
$R = 2$ tail u/v vectors		0.375 MiB
Base-plus-tail u/v history upper ledger		2.25 MiB
QKV activations		12.00 MiB

Table 6: Analytic storage ledger for the balanced banded $R = 2$ path at $L = 16384$, $W = 1024$, $B = 128$, $d = 64$ in float32. The first two rows quantify logical plan-factor materialization; the resident-tile row reflects the streaming block schedule. This is not a measured TPU HBM profile.

Projective contraction diagnostics on Pfam checkpoints. Table 7 reports the Birkhoff–Hopf certificate from Proposition 4 on the local Pfam test shards for the step-0 and step-1437 Sinkhorn checkpoints. For each strictly positive active 128-row block we compute the exact projective-diameter coefficient $\rho_H = \tanh^2(\Delta/4)$ on the scaled scores at $\varepsilon = 1$, excluding masked rows and columns. We also report the coarser range-only sufficient bound $\rho_{\text{range}} = \tanh^2(\Omega/2)$. Across 228 active blocks from 100 held-out examples, both certificates remain nontrivial; the final checkpoint has median $\rho_H = 0.241$ and maximum $\rho_H = 0.590$. The increase from step 0 to step 1437 indicates that

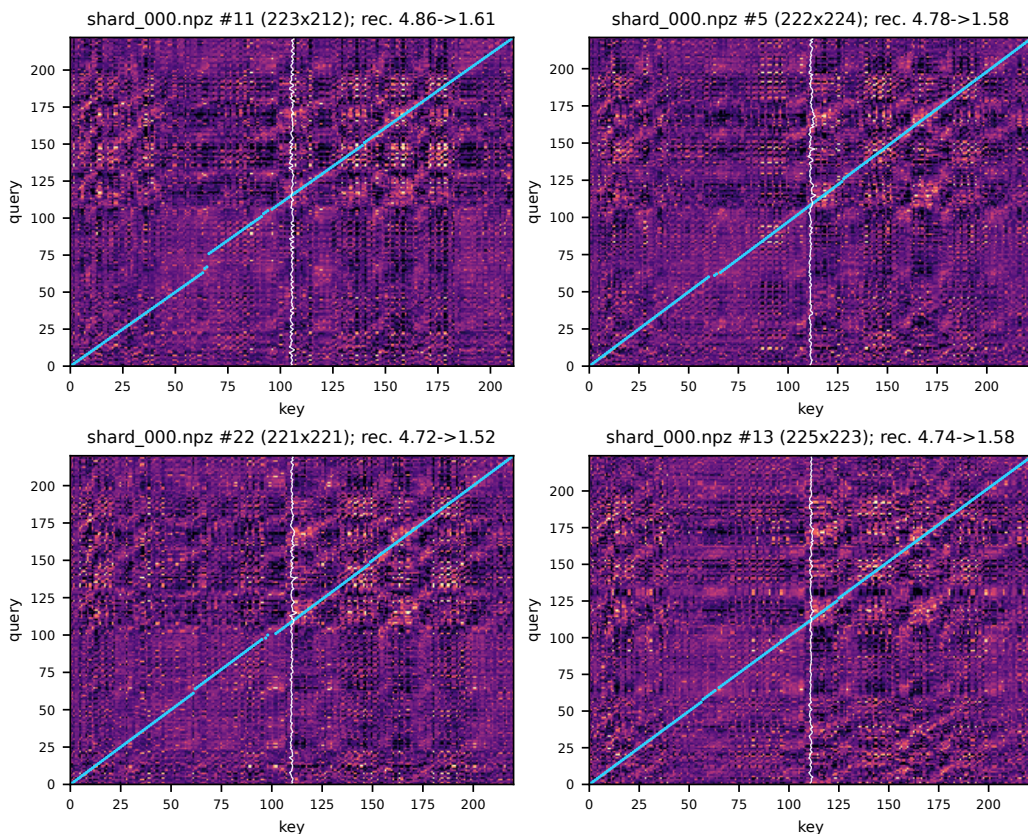


Figure 4: Multiple qualitative Pfam/ESM-2 checkpoint examples selected by local reconstruction-MSE improvement. Each panel shows the final-checkpoint tail-refinement transport plan, supervised target columns in cyan, and the plan barycenter in white. Panel titles report sequence lengths and step-0 to step-1437 reconstruction MSE.

the trained projections operate at higher score contrast, while remaining inside the locally contractive positive-block regime measured by the certificate.

Step	Blocks	Median ρ_H	P95 ρ_H	Max ρ_H	Median ρ_{range}	Max ρ_{range}
0	228	0.0748	0.296	0.345	0.282	0.582
1437	228	0.241	0.532	0.590	0.482	0.721

Table 7: Production-checkpoint projective contraction diagnostics on local Pfam test shards. The exact projective certificate is computed from the active block score matrix; the range-only bound is the simpler sufficient bound stated in Proposition 4.

Compact Pfam diagnostic visual summary. Figure 5 visualizes two local empirical summaries requested by the review. The left panel converts the step-50 screen table into a column-normalized heatmap, so the short-screen comparison across loss, sparse CE, monotonicity, and throughput is visible at a glance. The right panel shows the full ρ_H distribution underlying Table 7; it indicates higher learned score contrast, hence weaker but still bounded local contraction margins, rather than improved contraction.

D Kernel-Oriented Pseudocode

Balanced stopped-base and $R = 2$ tail.

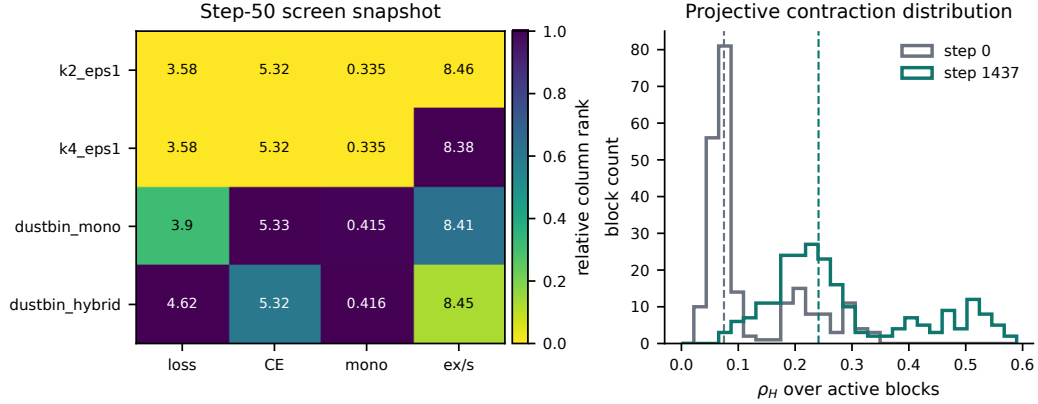


Figure 5: Compact Pfam diagnostic summaries. Left: relative column ranks for the short TPU screen metrics, with annotated raw values. Right: exact projective contraction coefficient distributions over active blocks at the step-0 and step-1437 checkpoints.

1. Form masked scaled scores $S_{ij} = Q_i K_j^\top / (\sqrt{d} \varepsilon)$ on the active support Ω .
2. Run the balanced masked Sinkhorn half-steps for T stopped iterations to obtain the base pair $(u^{(0)}, v^{(0)})$.
3. Recompute two differentiable refinement steps from the stopped base pair, producing $(u^{(1)}, v^{(1)})$ and $(u^{(2)}, v^{(2)})$.
4. Materialize only the base staircase plan $P^{(2,2)}$ blockwise.
5. Reconstruct $P^{(2,1)}$, $P^{(1,1)}$, and $P^{(1,0)}$ by row and column rescaling of $P^{(2,2)}$ using the dual differences $(u^{(a)} - u^{(2)}, v^{(b)} - v^{(2)})$. When using stored centered potentials, include the scalar gauge factors from the centered gauge ledger or reconstruct in a gauge-consistent raw representative.
6. Evaluate the exact $R = 2$ score-space VJP from Propositions 1 and 2, then propagate to (Q, K, V) .

Dustbin-augmented bridge.

1. Append one active dustbin token per side together with inactive fillers to construct the augmented tensors $(\tilde{Q}, \tilde{K}, \tilde{V})$.
2. Augment the masks analogously and enlarge the effective band width to $\tilde{W} = \max(W, L)$.
3. Apply the same balanced stopped-base and $R = 2$ tail procedure on the augmented state space.